Energy & Environmental Science

ROYAL SOCIETY OF CHEMISTRY

PAPER

View Article Online
View Journal | View Issue

Cite this: *Energy Environ. Sci.*, 2025, **18**, 4740

Robust interphase derived from a dual-cation ionic liquid electrolyte enabling exceptional stability for nickel-rich layered cathodes†

Fanglin Wu,[abc] Haolin Tang,[*a] Jian Wang,[bc] Xilai Xue,[bc] Thomas Diemant,[bc] Shan Fang,[d] Huihua Li,[bc] Ziyuan Lyu,[bc] Hao Li,[a] En Xie,[a] Hongzhen Lin,[e] Jae-Kwang Kim,[f] Guk-Tae Kim*[bcfg] and Stefano Passerini[*bch]

Nickel-rich layered cathodes suffer from unstable interfaces and structural collapse, leading to poor cycling stability in conventional carbonate-based electrolytes. Ionic liquid electrolytes have the potential to enable high-safety and high-specific energy in lithium metal batteries employing nickel-rich cathodes. However, their practical performance is limited by their low ionic conductivity and unsatisfactory interphase formation, which allow operation only at relatively low current densities. In this work, a dual-cation-IL-based electrolyte was employed comprising $NaPF_6$ as an additive for tuning the solvation structure. This electrolyte, which exhibited high ionic conductivity (5.06 mS cm^{-1} at 20 °C), enabled Li||$LiNi_{0.83}Co_{0.11}Mn_{0.05}B_{0.01}O_2$ cells operating in the voltage range of 3.0–4.3 V with excellent capacity retention after 500 cycles at 1 C (95.2%) and a 1500-cycle-long lifespan (>80%). Even after reducing the operative temperature to 0 °C, the cells could deliver high discharge capacity (above 150 mA h g^{-1}) at 0.5C without capacity decay. *Ex situ* X-ray photoelectron spectroscopy and time-of-flight secondary-ion mass spectrometry analyses revealed that the electrode/electrolyte interphase derived from the $NaPF_6$ additive was more robust and uniform, possibly facilitating sodium co-deposition on the anode surface against Li dendrite growth. Meanwhile, the inorganic-dominated cathode/electrolyte interphase (CEI) considerably protected the cathode structure and inhibited lattice distortion and microcracks, as revealed by atom-level electron microscopy and *in situ* X-ray diffraction.

Received 5th February 2025,
Accepted 26th March 2025

DOI: 10.1039/d5ee00669d

rsc.li/ees

Broader context

High-specific-energy rechargeable lithium batteries are being fiercely studied by researchers and battery makers to meet the ever-increasing demands for extended driving ranges in electric vehicles and electric vertical take-off and landing (eVTOL) aircrafts. However, the most pressing task is to ensure high safety using an exceptionally stable electrolyte to eradicate the risks of battery ignition or explosion. In recent years, ionic-liquid-based electrolytes (ILEs) have been proposed as potential replacements for conventional highly flammable carbonate-based electrolytes, especially for lithium metal batteries (LMB). However, the inferior ionic conductivity of ILEs at ambient temperatures limits the rate performance of the resulting cells. Herein, a highly ion-conducting dual-cation IL-based electrolyte comprising the $NaPF_6$ additive was developed, which afforded LMBs with a 1500-cycle-long lifespan at 1C (>80%) and room temperature or 0 °C using high-voltage, nickel-rich positive electrodes. This study highlights the possibility of employing ILEs in practical LMBs to realize high safety and long-term cycling.

[a] *State Key Laboratory of Advanced Technology for Materials Synthesis and Processing, Wuhan University of Technology, Wuhan, Hubei 430070, China. E-mail: thln@whut.edu.cn*
[b] *Helmholtz Institute Ulm (HIU), Helmholtzstrasse 11, Ulm 89081, Germany. E-mail: guk-tae.kim@kit.edu, stefano.passerini@kit.edu*
[c] *Karlsruhe Institute of Technology (KIT), P.O. Box 3640, Karlsruhe 76021, Germany*
[d] *School of Physics and Materials Science, Nanchang University, Nanchang, Jiangxi, 330031, China*
[e] *i-Lab & CAS Key Laboratory of Nanophotonic Materials and Device Suzhou Institute of Nano-Tech and Nano-Bionics, Chinese Academy of Sciences, Suzhou, Jiangsu 215123, China*
[f] *Department of Energy Convergence Engineering, Cheongju University, Cheongju, Chungbuk, 28503, Republic of Korea*
[g] *Il Chem Co., Ltd, 282, Hagui-ro, Dongan-gu, Anyang-si, Gyeonggi-do, Republic of Korea*
[h] *Austrian Institute of Technology (AIT), Center for Transport Technologies, Giefinggasse 4, 1220, Wien, Austria*

† Electronic supplementary information (ESI) available. See DOI: **https://doi.org/10.1039/d5ee00669d**

1. Introduction

High-specific-energy rechargeable lithium batteries hold great potential in the development of electric vehicles, promising to deliver a longer driving range and relieve charging anxiety. Presently, cathode materials mainly restrict the energy performance of cells because of their lower theoretical specific capacity than those of silicon/graphite and, potentially, lithium metal anodes.[1,2] Nickel-rich layered oxides $LiNi_xCo_yMn_{1-x-y}O_2$ (NCM, $x \geq 0.8$) have been at the forefront of promising cathode candidates in virtue of their high specific capacity and working voltage and low cost.[3,4] Nevertheless, nickel-rich materials exhibit poor cycling stability[5] and thermodynamic instability[6] in conventional carbonate-based electrolytes owing to the highly reactive Ni^{4+} ions, which are easily reduced to Ni^{2+}/Ni^{3+} by carbonate solvents (*e.g.*, ethylene carbonate), simultaneously causing the decomposition of solvent molecules.[7,8] Furthermore, these cathodes suffer from cation mixing between Ni^{2+} and Li^+, resulting in the formation of the inactive rock-salt phase starting from the surface of the outer secondary particle and progressing into their bulk along the boundary of primary particles. This process is accompanied by severe microcracks in the cathode secondary particles, which further increase the Li^+ charge transfer resistance and aggravate performance decay.[9,10] Construction of highly robust cathode/electrolyte interphases (CEIs) *via* electrolyte engineering has gained widespread recognition because it can suppress the performance degradation of nickel-rich cells by sustaining the structural integrity of cathode particles.[11–13] Conventional carbonate-based electrolytes generally form a non-uniform, organic-rich CEI layer accompanied by a high resistance and poor capability making to mitigate side reactions between the electrolyte and cathode.[14] In comparison, inorganic-rich species, typically represented by lithium fluoride (LiF), have been demonstrated to facilitate uniform and rapid transportation of lithium ions across electrode/electrolyte interfaces by enhancing electronic insulation and ionic conduction and thereby avoiding unceasing electrolyte decomposition.[15–17] The electrolyte plays a critical role in determining the electrode/electrolyte interface chemistry.[18,19] Undoubtedly, rationally designing inorganic-rich electrode/electrolyte interphases *via* electrolyte engineering is a feasible route to achieve high-performance nickel-rich lithium batteries.

In recent years, ionic liquid electrolytes (ILEs) were revealed to yield dense inorganic-rich CEI, enabling highly stable lithium metal batteries coupled with high capacity nickel-rich- and lithium-rich-cathodes.[9,20] The underlying reason is the highly stable electrode/electrolyte interphases composed of LiF-dominated inorganic products, which protect cathode materials against an attack from acidic species in electrolytes.[21] Furthermore, it should be emphasized that the intrinsic properties of ILEs, *e.g.*, non-flammability, low volatility and a broad electrochemical stability window (ESW), make them promising as highly safe electrolytes for next-generation lithium metal batteries.[22,23] Despite their potential, the low ionic conductivity of common ILEs remains a significant obstacle to their practical applications, particularly under high-rate-performance and low-temperature conditions. Among ILEs, ethylmethylimidazolium (EMI)-based ILEs are promising candidates because they exhibit ionic conductivities close to those of carbonate-based electrolytes, *e.g.* 1-ethyl-3-methylimidazolium bis(fluorosulfonyl)imide (EMIFSI) can achieve an impressive ionic conductivity of 7.71 mS cm^{-1} at 20 °C.[24] However, these types of ionic liquids have poor compatibility with lithium metal, leading to lower electrochemical stability. This limitation hampers the further development of EMI-based ILEs, restricting them from becoming the mainstream option in high-voltage lithium metal batteries.[25] Their poor cathodic stability is ascribed to the reactivity of the proton at the C-2 position in the imidazolium ring, which forms N-heterocyclic carbenes after the prolonged contact of ILs with lithium metal.[26] Fluoroethylene carbonate (FEC) can form a protective solid electrolyte interphase (SEI) layer that prevents direct contact between the EMI cation and lithium metal, thus alleviating subsequent decomposition reactions associated with ionic liquids.[26] Anions also have a significant effect on the interfacial stability between the EMI cation and lithium metal anode. Takafumi *et al.* compared different anions, specifically bis(fluorosulfonyl)imide (FSI) and bis(trifluoromethanesulfonyl)imide (TFSI), and demonstrated that FSI^- imparts superior stability than $TFSI^-$ when used in combination with the EMI cation and sodium metal anode.[27] Additionally, functionalizing the imidazolium cation[28] and using high-concentration ILEs[25] can effectively enhance the stability of EMI-based ILs in lithium metal batteries. Nevertheless, in these routes, it is arduous to fully block the side reactions of EMI cations.

In this study, we present a novel electrolyte engineering approach to realize the exceptional stability of lithium metal batteries comprising EMI-based ILEs. The competitive functions of 1-butyl-1-methylpyrrolidinium (Pyr_{14}^+) and the electrolyte additive $NaPF_6$ fully isolate the reduction of EMI cations against lithium metal while enabling the formation of a reinforced CEI that strongly protects the integrity of the cathode structure, thus guaranteeing outstanding electrochemical performance. Consequently, this study highlights the feasibility of using EMI-based ILEs and provides a novel strategy to simultaneously achieve high stability and high rate capability in lithium metal batteries.

2. Results and discussion

Electrochemical stability, a crucial benchmark of electrolytes for their use in high-voltage battery chemistries, can be evaluated *via* linear sweep voltammetry (LSV). To assess the influence of dual cations (Pyr_{14}^+ and EMI^+) compared with that of pure EMI cations, the LSV curves of a pure EMI cation-based ILE (0.2LiFSI–0.8EMIFSI, named PEIL) and a hybrid ILE (0.2LiFSI–0.4EMIFSI–0.4Pyr_{14}FSI, named HEIL) are displayed in Fig. 1a. At a threshold for oxidation of 2.5 μA cm^{-2}, a very low value compared with most previous studies, the increase in the current around 4 V in the LSV curve of the PEIL indicates the onset of the oxidation reaction occurring at the platinum electrode. Compared with the HEIL, where the EMI cation is

partially replaced by the Pyr_{14} cation, the current increases more gradually, crossing the oxidation threshold at ~4.5 V. Although unexpected, the presence of the Pyr_{14} cation clearly contributes to the enhancement in the anodic stability of the electrolyte, which can be attributed to the larger steric hindrance of the alkyl group that forms a thicker double-layer and overscreens anions from oxidation.[29,30] However, the larger steric hindrance of the Pyr_{14} cations inevitably impairs the lithium transport ability. To evaluate this effect of Pyr_{14}^+ addition, the ionic conductivity of the PEIL and HEIL at different temperatures is displayed in Fig. 1b. A relatively high ionic conductivity of 5.85 mS cm^{-1} is observed for the HEIL at 20 °C, which is slightly lower than that of the PEIL (7.52 mS cm^{-1}). Still, the HEIL exhibits ionic conductivities of 2.37 and 0.62 mS cm^{-1} at 0 and −20 °C, respectively. This indicates that the dual-cation-based HEIL exhibits high conductivity at room temperature and sub-ambient temperatures. To verify the effect of Pyr_{14}^+ addition on the electrochemical performance of lithium metal batteries, the cycling behaviours of PEIL- and HEIL-based Li||NCM83 cells are compared in Fig. 1c and Fig. S1 (ESI†).

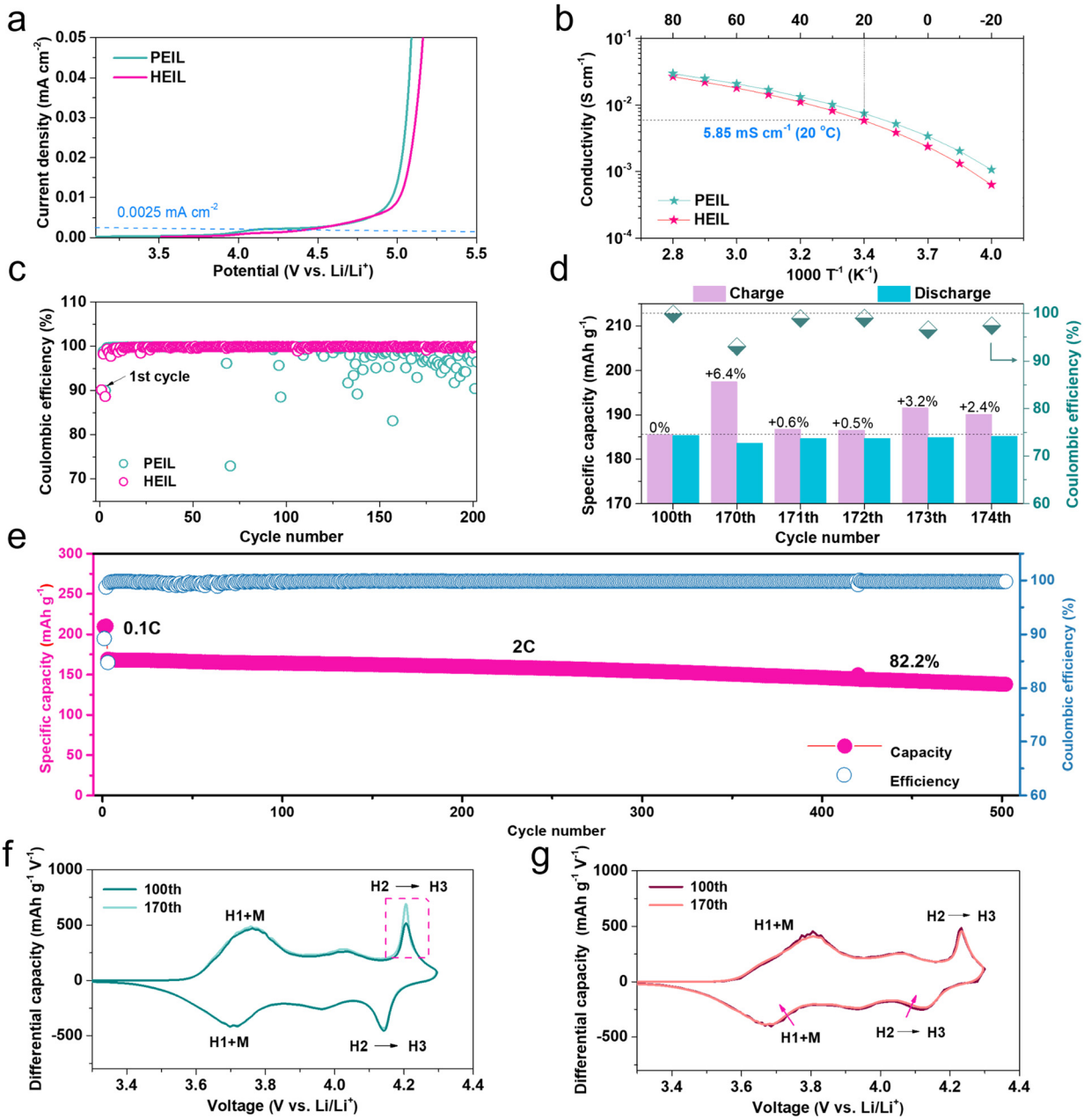

Fig. 1 (a) LSV curves of PEIL and HEIL electrolytes at a scan rate of 0.1 mV s^{-1}. (b) Ionic conductivity of the HEIL electrolyte. (c) Coulombic efficiency of Li||NCM83 cells using the PEIL or HEIL upon cycling at 1C and 20 °C. (d) Detailed specific capacities of the PEIL-based Li||NCM83 cell from the voltage curves presented in Fig. S4 (ESI†). (e) Long-term cycling behaviour of Li||NCM83 cells in the HEIL at 2C. Comparison of differential capacity curves in the 100th and 170th cycle for cells with the (f) PEIL and (g) HEIL electrolytes.

No significant difference is observed in the first cycle (Fig. S2, ESI†); the PEIL cell delivers a discharge capacity of 210 mA h g^{-1}, which is slightly lower than that of the HEIL cell. While the discharge capacity of the PEIL cell stays relatively stable during the subsequent 200 cycles, large fluctuations and, eventually, degradation of coulombic efficiency (CE) are observed after approximately 120 cycles, with the CE hardly returning to 99% upon further cycling (Fig. 1c). The change in the CE upon prolonged cycling (500 cycles) is displayed in Fig. S3 (ESI†), confirming that the low CE of the PEIL cell is persistent, indicating that the side reactions of the ILE continuously occur in the cell during its cycling. To further analyse the underlying reasons for this behaviour, the selected voltage profiles after specific cycle numbers are presented in Fig. S4 (ESI†). While the discharge curves are almost consistent, an obvious discrepancy is observed in the charge curves at high voltages, which extends to larger values with increasing cycle numbers. This is probably due to the decomposition of FSI^- anions or the growth of soft dendrites, as evidenced by the SEM images of cycled lithium metal (Fig. S5, ESI†), which show numerous pits on the metal surface and fluffy-like dendrites growing from these pits, leading to the larger charge capacity that dramatically decreases the CE.[31,32] The charge/discharge capacities and CE values of the PEIL-based cell after several selected cycles are compared in Fig. 1d. There is no significant variation in the discharge capacity, but the charge capacity shows significant fluctuations. In contrast, the HEIL cell maintains high CE values, close to 100%, during cycling (Fig. 1c and Fig. S3, ESI†), and the HEIL cell exhibits stable cycling performance for 500 cycles. Even at a high rate (2C), the cell still maintains high cycling stability with a capacity retention of 82.2% after 500 cycles (Fig. 1e). Generally, the electrochemical behaviour is associated with phase transitions occurring on the surface and bulk of the cathode.[33] To further understand the fluctuating CE, the differential capacity curves of PEIL- and HEIL-based Li||NCM83 cells are compared in Fig. 1f and g. A sharp increase in the peak corresponding to the H2–H3 phase region is observed in the differential capacity curve of the PEIL-based cell. This region reflects the transformation of the crystalline structure from the hexagonal H2 solid solution phase to the H3 solid solution phase, accompanied by lattice contraction, which cannot contribute to an increase in the peak intensity. Therefore, the abrupt peak growth can be ascribed to the flattening of the voltage plateau at which the process occurs. In contrast, the H2–H3 peak in the differential capacity curve of the HEIL-based cell does not abruptly change, but a slight peak shrinkage during the reduction process is observed (Fig. 1f), which indicates mild performance degradation upon cycling (Fig. S1, ESI†). The capacity retention of this cell is 94.3% after 200 cycles, which indicates the imperfect performance of the electrode/electrolyte interphases and/or the corrosion of the current collector in the full FSI anion ILE system.[34] The $LiPF_6$ salt is the most common lithium salt, and it exhibits certain defects, such as poor thermal stability. However, it can excellently suppress the corrosion of the Al current collector.[35] More importantly, PF_6^- anions are known to contribute to the formation of a fluorine-rich cathode/electrolyte interphase.[36,37] Furthermore, sodium ions can promote homogenous lithium deposition *via* co-deposition on the anode surface, hindering lithium dendrite growth.[38,39] Therefore, $NaPF_6$ was introduced as an additive into the HEIL to tune the interfacial chemistry at both electrodes of the Li||NCM83 cell.

The novel electrolyte was prepared by dissolving $NaPF_6$ and LiFSI (mole ratio = 1 : 9) in an equimolar mixture of EMIFSI and $Pyr_{14}FSI$ to obtain $0.2NaPF_6$–1.8LiFSI–4EMIFSI–$4Pyr_{14}FSI$, henceforth called NaEIL. The stripping/plating behaviour of the NaEIL and HEIL on lithium metal anodes at different current densities is compared in Fig. 2a. At a low current density (0.1 mA cm^{-2}), no significant difference is observed between the symmetric Li cells employing the HEIL and NaEIL. Initially, the potential of the cell with the NaEIL is slightly higher than that of the cell with the HEIL, probably due to the partial replacement of lithium ions by larger sodium ions, leading to a slightly reduced Li^+ ion transport ability.[40] This is also confirmed by their measured ionic conductivity at different temperatures (Fig. S6, ESI†), where a slightly lower ionic conductivity is observed for the NaEIL-based cell than the HEIL-based cell (*e.g.*, 5.06 *vs.* 5.85 mS cm^{-1} at 20 °C). However, when the current density is increased to 0.2 mA cm^{-2}, obvious fluctuations occur in the voltage of the HEIL-based cell at approximately 100 h, indicating the occurrence of partial short circuits inside the cell. Subsequently, the cell voltage decreases upon cycling even with an increase in the current density, demonstrating the occurrence of short circuits due to Li dendrite deposition. In contrast, the cell using the NaEIL exhibits a stepwise increase in the voltage with increasing current density, which gradually stabilizes with cycling at the same current rate, indicating the absence of Li dendrites, *i.e.*, the formation of a stable electrode/electrolyte interphase. To further evaluate the electrochemical behaviour of the electrolyte with and without the $NaPF_6$ additive at high current densities, prolonged stripping/plating cycling tests at 0.5 mA cm^{-2} were performed for both electrolytes. The electrochemical impedance spectroscopy (EIS) results of the cells comprising the two electrolytes before cycling display consistent interfacial resistance (Fig. 2b), suggesting that the sodium-containing additive does not induce any additional spontaneous reaction upon contacting the lithium metal surface. After the stripping/plating cycling test (Fig. 2c), the HEIL electrolyte shows a fast and continuous decrease in the overpotential until the occurrence of a full short circuit after approximately 100 h, as evidenced by the square-wave-like overpotential in Fig. S7a (ESI†) and Fig. 2d. The almost-zero resistance further confirms the dendrite short circuit in the HEIL (Fig. S7b, ESI†). In contrast, the NaEIL electrolyte exhibits a steadier overpotential. The resistance almost does not change compared with the value before cycling (Fig. S7c, ESI†). Even after 400 h, the cell maintains a stable overpotential, as shown in Fig. 2d. To evaluate the influence of the $NaPF_6$ additive on the electrochemical stability of the IL-based electrolyte, the NaEIL was subjected to LSV measurements, as shown in Fig. S8 (ESI†). The electrochemical stability window is slightly broadened by the presence of the additive, revealing that $NaPF_6$ does not diminish the anodic stability of the NaEIL but reinforces its oxidation resistance ability. In the next

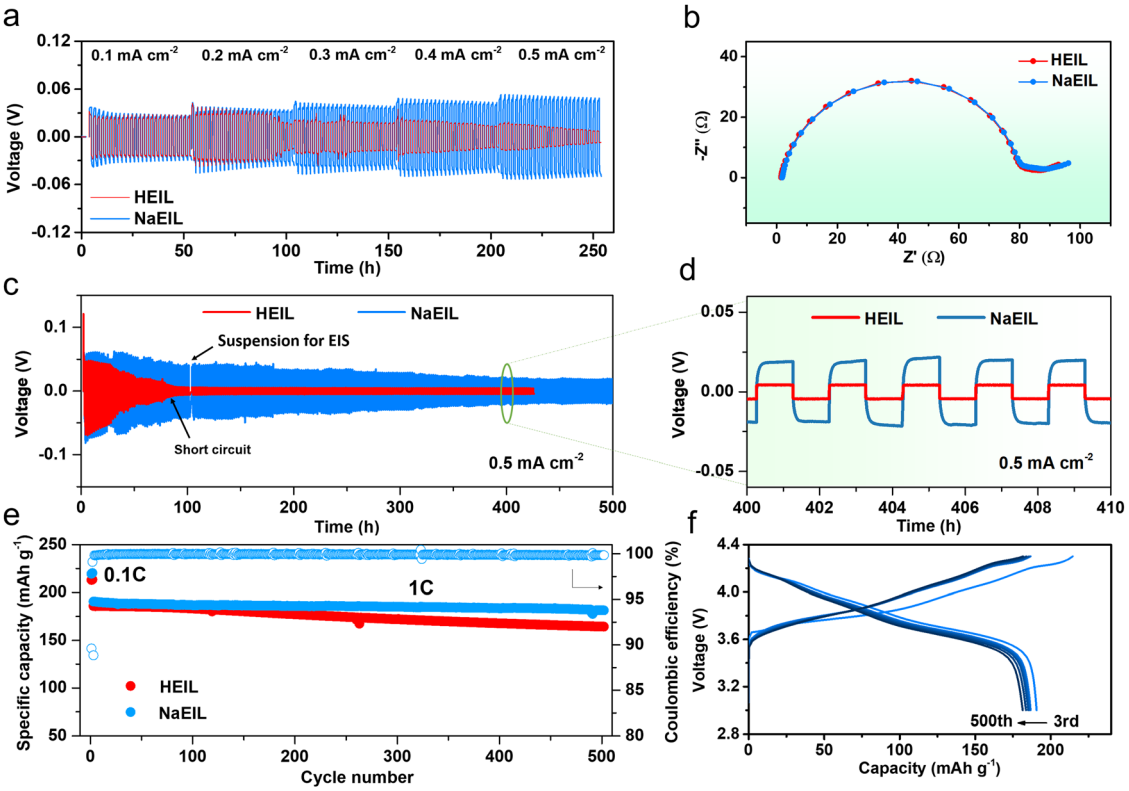

Fig. 2 (a) Stripping/plating behaviour of symmetric Li||Li cells with the HEIL and NaEIL at different current densities. (b) EIS spectra of the HEIL and NaEIL before cycling at 0.5 mA cm^{-2}. (c) Stripping/plating behaviour of symmetric Li||Li cells in the HEIL and NaEIL at 0.5 mA cm^{-2}, and its (d) enlarged section. (e) Long-term cycling performance of Li||NCM83 cells in the EIL and NaEIL at 1C and 20 °C and the (f) corresponding selected voltage curves within the cycle range from 3 to 500 in NaEIL.

step, Li||NCM83 cells with the two electrolytes were assembled to assess their electrochemical performance. Compared with the HEIL-based cell, the NaEIL-based cell shows a slightly higher initial discharge capacity during the activation process at 0.1C (the corresponding voltage profiles are shown in Fig. S9, ESI†), while its CE is comparable. At 1C, both cells deliver similar discharge capacities. However, the capacity retention after 500 cycles clearly improves from 88.4% for the HEIL-based cell to 95.2% for the NaEIL-based cell. Additionally, the voltage evolution after the cycling of the NaEIL-based cell demonstrates remarkable stability (Fig. 2f), whereas a stronger performance decay is observed for the HEIL-based cell (Fig. S10, ESI†). This impressively high cycling stability confirms the beneficial effect of the addition of $NaPF_6$ to the electrolyte.

The difference in electrochemical performance generally originates from the morphology and microstructure of electrodes. To investigate the effect of $NaPF_6$ on the lithium metal anode, the surfaces of the lithium electrodes extracted from symmetric cells were analysed *via* SEM (Fig. S11, ESI†). While a fluffy-like layer and several dendritic filaments are observed on the Li surface after cycling with the HEIL electrolyte (Fig. S11a, ESI†), a distinctly different morphology is observed after cycling with the NaEIL electrolyte (Fig. S11b, ESI†). More precisely, a denser, globular coverage is observed on the lithium metal surface. The elemental distribution, obtained using energy-dispersive X-ray spectroscopic (EDX) mapping, reveals that the coating layer formed on the electrode in the NaEIL-based cell is rich in inorganic sulfide- and fluoride-based products (Fig. S11c, ESI†). Additionally, EDX mapping shows the homogenous distribution of sodium on the lithium surface. Although sodium only accounts for a low weight ratio of surface species, its participation in the formation of the SEI layer is evident. The larger sodium ions prefer to co-deposit at lithium protuberance sites, which suppresses the growth of lithium dendrites.[38,39,41] Compared with the anode, the microstructure of the cathode also plays an important role in the cycling stability of cells. Therefore, the structure and surface chemistry of the cathode after cycling were also comprehensively studied. In particular, advanced spherical-aberration-corrected scanning transmission electron microscopy (Cs-STEM) was employed to understand structural evolution during cycling. Furthermore, cycled NCM83 secondary particles were cut using a focused ion beam (FIB) to observe their internal structures. In general, the particles cycled with either the HEIL or NaEIL exhibit good structural integrity after 200 cycles (Fig. S12, ESI†). However, mild microcracks are observed in the particles cycled in the HEIL, whereas no damage is observed in the particles cycled in the NaEIL.

The primary particles embedded in the secondary particles after 200 cycles in both electrolytes are well visible in the STEM images (Fig. S13, ESI†). The high-angle annular dark-field (HAADF) images reveal that the polygon-shaped primary

particles have a size of <1 μm. To obtain more information on the outer surface of the primary particles, the analysis focused on the edge area (red rectangle, Fig. S13c, ESI†) to observe the crystal fringes more in detail (Fig. 3a). First, a thin layer ($\sim$8 nm thick) is observed on the surface of the particle cycled in the HEIL, which is mainly composed of amorphous species and the rock-salt NiO phase, as observed in the magnified image of region I (in Fig. 3b). Then, in the bulk of the particle, a NiO layer ($\sim$2 nm thick) is observed. The fast Fourier transform (FFT) image of region I verifies the rock salt structure of the outer layer (Fig. 3c). In contrast, the inner part of the particle (region II) still maintains a well-ordered hexagonal phase (Fig. 3d). The integrated EDX elemental mapping for F, Ni and Co (Fig. 3e and Fig. S14, ESI†) of the outer layer demonstrates that it is mainly composed of nickel rather than fluorine. Such a reconstructed inactive NiO layer may be unfavourable for Li^+ transport.[42,43]

Next, the edge of the cathode particle cycled in the NaEIL was characterized (Fig. 3g). In this case, a $\sim$2-nm spinel or rock-salt phase layer is observed at the outer layer of the primary particle. Additionally, a thin dark layer is observed on the topmost particle surface, which is visible more clearly in the HAADF image (Fig. S15, ESI†). This amorphous layer is 2–3 nm thick and shows a strong fluorine signal in EDX mapping (Fig. 3k and l), demonstrating the formation of a fluorine-rich CEI on the NCM83 primary particles. In contrast, no nickel signal is detected in the topmost surface layer. The individual elemental mappings further confirm the lack of transition metal ions in the topmost surface layer (Fig. S15, ESI†). Additionally, the EDS mapping for phosphorus reveals that this layer is not only fluorine-rich, but also contains a significant amount of phosphorous. Therefore, it can be concluded that an F- and P-rich CEI is formed on the surface of the NCM83 particles upon cycling in the NaEIL, which enhances the structural stability upon long-term cycling. The well-ordered layer structure (Fig. 3h, selected from region III) demonstrates that the hexagonal structure remains intact, with a lattice distance of 0.49 nm (Fig. 3j). Moreover, the very thin and uniform 5–6-atomic-layer thick spinel or rock-salt phase ($\sim$2 nm) may contribute to the enhanced structural stability.

To further analyse the chemical composition of the components on the surface of cathode particles, X-ray photoelectron spectroscopy (XPS) was performed before and after ion sputtering. The cycled electrodes were rinsed with dimethyl carbonate (DMC) before measurements and then transferred to the XPS chamber without contacting ambient air. The detailed spectra in the C 1s, O 1s and F 1s regions of the electrodes are exhibited in Fig. 4a–c while those in the N 1s and P 2p regions are shown in Fig. S16 and S17 (ESI†). In the C XPS spectrum of the NaEIL electrode, a stronger peak is detected at approximately 290.5 eV,

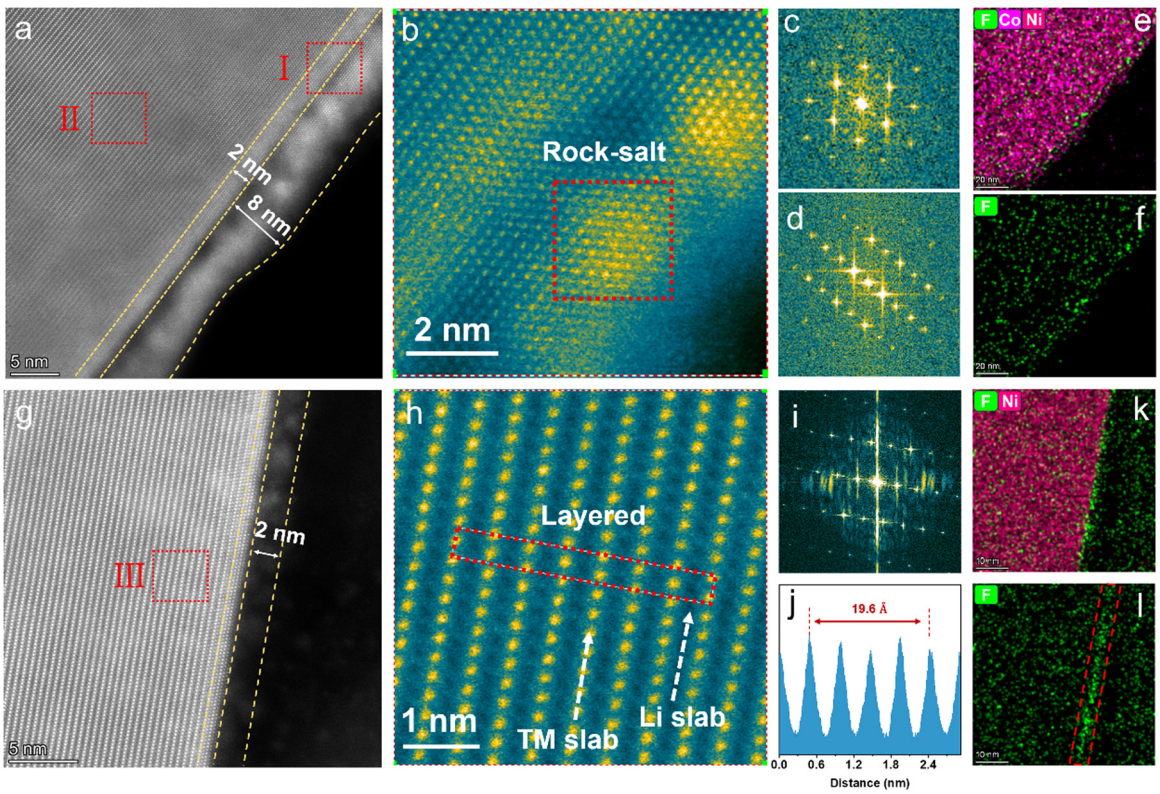

Fig. 3 STEM-HAADF images and corresponding results in (a)–(f) HEIL and (g)–(l) NaEIL. (a) STEM image of the NCM83 electrode after 200 cycles in HEIL. (b) Magnified image of region I in Fig. 3a. FFT images of (c) region I and (d) region II in Fig. 3a. EDX mappings of (e) F, Co, and Ni elemental distributions and (f) individual F elemental distribution. (g) STEM images of the NCM83 electrode after 200 cycles in NaEIL. (h) Magnified image, (i) FFT image and (j) intensity line profile of region III in Fig. 3g. EDX mappings for (k) F and Ni elemental distributions and (l) individual F elemental distribution.

which is assigned to C–F species in the NaEIL electrode (bottom, Fig. 4a–c), compared with the HEIL electrode (top, Fig. 4a–c), probably originating from the PVdF binder. The less-intense peak of C–N/C–O species at 286.3 eV indicates the reductive decomposition of the cations of the IL. Combining the significantly lower characteristic peaks of the IL and its decomposition products in the N 1s (Fig. S16, ESI†), it can be deduced that the IL's decomposition is much less pronounced for NaEIL than for HEIL. The peak at ~531.8 eV in the O 1s region can be attributed to C═O from carbonates, originating from the rinsing with DMC, and S═O from sulphates, formed due to the decomposition of FSI anions. However, this peak is much stronger in the XPS spectrum of the electrode cycled in the NaEIL than in the HEIL, which indicates the presence of a higher concentration of sulphates on the NaEIL surface. Additionally, an obviously stronger peak of LiF is observed in the F 1s spectrum of the electrode cycled in the NaEIL. These inorganic species are mechanically stiff, excellent ion conductors, and poor electronic conductors, contributing to the formation of a robust, functional CEI. The XPS analysis was complemented with time-of-flight secondary ion mass spectrometry (ToF-SIMS) measurements to determine the products on the particle surface from a three-dimensional (3D) perspective. The distribution of fluorine ions (mainly LiF) is more uniform after cycling with the NaEIL; after cycling in this electrolyte, a higher fluorine concentration is detected on the electrode surface (Fig. 4d), which further indicates the formation of a more homogenous and robust CEI layer. To determine the origin of this difference, 3D images of Na^+ and PF_6^- distributions in the CEI formed with the NaEIL are shown in Fig. 4e and f. The rare distribution of Na^+ and PF_6^- implies that these ions are not directly involved, to a larger degree, in the formation of the CEI layer. In contrast, the 3D images of PO_2^- species (Fig. 4g) show the decomposition of PF_6^- into phosphates (also corroborated by the P 2p XPS detailed spectrum in Fig. S17, ESI†) and LiF and the integration of these products into the CEI layer, which results in the high concentration of LiF (Fig. 4h). The 3D images of SO_4^- demonstrate the much higher concentration of inorganic sulphates from the outer surface of the particle to its inner layer (Fig. 4i), which originates from the decomposition of the FSI anion. This is also consistent with the above-given XPS results (Fig. 4b). The corresponding depth profiles of the intensity of F^- and SO_4^- are displayed in Fig. 4j and k. These indicate that the fluorine and sulphate concentrations after cycling are much higher in the top layer in the NaEIL-cycled electrode (*i.e.*, near the electrolyte) than the HEIL-cycled electrode. Furthermore, higher contents of fluorine and sulphates are maintained with the depth of CEI layer in the former than the latter. Inorganic products such as fluorides, phosphates and sulphates are known to contribute to a more stable electrode/electrolyte interphase,[44–47] enhancing the structural stability of cathode particles during long-term charge/discharge cycling.

To evaluate the effect of the $NaPF_6$ additive on the crystalline structure of the cathode upon charge/discharge cycling, an

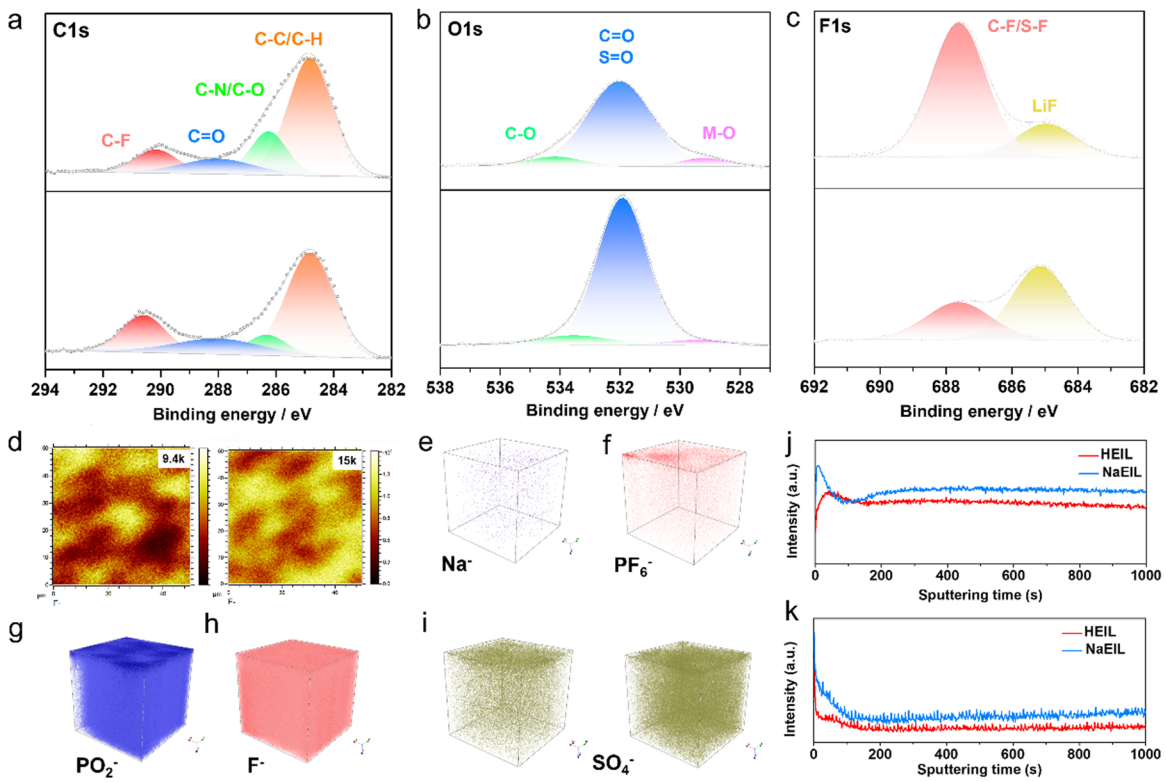

Fig. 4 Detailed XPS spectra of the (a) C 1s, (b) O 1s and (c) F 1s regions of NCM83 electrodes after 200 cycles in HEIL (top) and NaEIL (bottom). TOF-SIMS analysis of cycled NCM83 electrodes. (d) Mapping distribution of F ions in (left) HEIL and (right) NaEIL. 3D distributions of (e) Na^+, (f) PF_6^-, (g) PO_2^- and (h) F^- in NaEIL. (i) 3D distribution of SO_4^- in (left) HEIL and (right) NaEIL. Depth profiles of (j) F^- and (k) SO_4^-.

in-depth *in situ* XRD study was performed to monitor the phase evolution during the first charge/discharge cycle in both electrolytes. The primary reflections of (003) and (104) were selected to assess the variation in the *c*-lattice parameter of the $R\bar{3}m$ space group and the cation mixing in the layered structure. After charging the material in the HEIL (Fig. 5a), the (003) peak initially shifts to lower angles following the extraction of lithium ions from the cathode. However, a dramatic reversal, *i.e.*, a shift back to higher angles, is later observed, which is ascribed to the phase transformation from H2 to H3, where the delithiation inside the crystal structure leads to a corresponding variation in the *c* value. During the discharge process, the trend is reversed, with the (003) peak ending 0.15° lower than the initial angle. The maximum peak shift is approximately 0.81°. A similar behaviour is observed when using the NaEIL as the electrolyte (Fig. 5b), where the maximum peak shift (0.79°) is only slightly lower than that in the HEIL. However, the (003) peak shift after the first full charge/discharge cycle is comparatively small, only 0.04° in the NaEIL *versus* 0.15° in the HEIL. Similar results are observed for the (104) peak upon cycling in the NaEIL and HEIL (0.02° *vs.* 0.11°). To estimate the variation in the lattice, the *c* value and unit cell volume were calculated from Rietveld refinements. The results in Fig. S18 (ESI†) confirm smaller *c*-axis contraction and lower lattice volume variation in the NaEIL. The origin of such a lower peak shifting in the NaEIL is the higher stability of the CEI

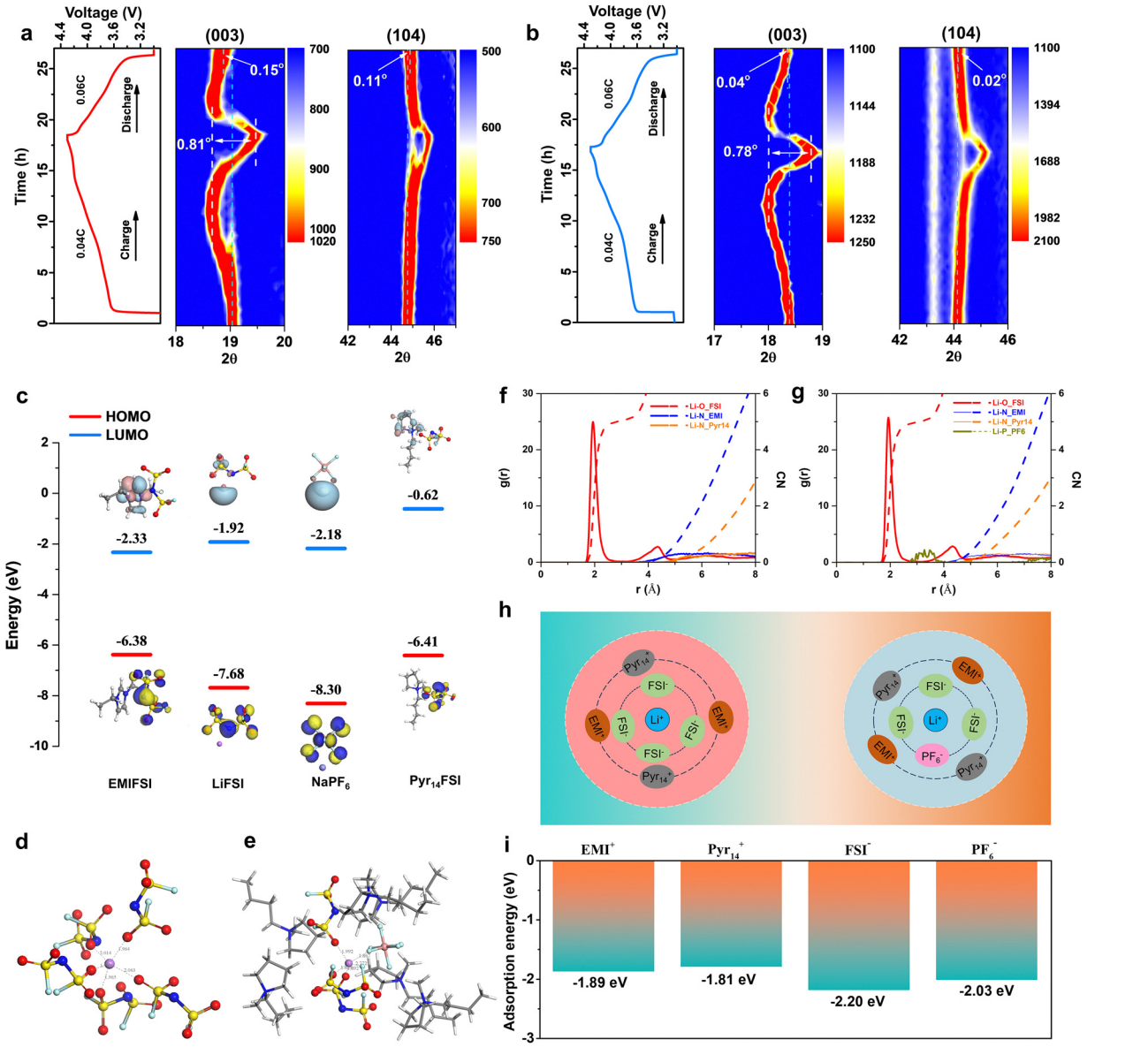

Fig. 5 Charge–discharge profile of the first cycle and the corresponding *in situ* XRD evolution of (003) and (104) main peaks in (a) HEIL and (b) NaEIL. (c) HOMO and LUMO energy levels of the investigated solvents and salts. Representative solvation structure of Li^+ in (d) HEIL and (e) NaEIL. Calculated RDFs and coordination numbers of Li^+ in (f) HEIL and (g) NaEIL. (h) Schematic of the solvation structures of Li^+ in HEIL (left) and NaEIL (right). (i) Adsorption energy of different ions on the lithium metal surface.

layer, which prevents the side reactions of highly reactive Ni^{4+} with electrolytes at high delithiation states and suppresses the Li^+/Ni^{2+} mixing on the surface of active material particles. Overall, this leads to lower mechanical strain along the *c*-axis, restraining the formation and propagation of microcracks in the NCM83 particles. These results highlight the role of $NaPF_6$ in stabilizing the cathode structure, which in turn suppresses performance degradation. To understand the effect of $NaPF_6$ from a molecular perspective, density functional theory (DFT) calculations in combination with molecular dynamics (MD) simulations were performed to identify the differences made by the additive on the electrolyte and, later, on the CEI. The highest occupied molecular orbital (HOMO) energy of $NaPF_6$ is obviously lower than those of the ionic liquid and lithium salts (Fig. 5c), confirming the enhanced oxidation resistance ability due to the addition of the $NaPF_6$ additive, in agreement with the LSV results (Fig. S8, ESI†). MD simulations reveal the solvation structures of ILEs with and without the $NaPF_6$ salt. Selected snapshots of the solvation structure are displayed in Fig. S19 (ESI†), which reveal that Li^+ ions are mainly surrounded by FSI^- anions (Fig. 5d and e). After the addition of $NaPF_6$, however, the first solvation shell is altered, containing FSI^- and PF_6^-. The radial distribution function (RDF; Fig. 5f and g) shows a prominent peak of FSI^- at ~2.0 Å in the Li^+ solvation shell, along with an additional peak related to PF_6^- at ~3.4 Å, suggesting that PF_6^- is also involved in the formation of the first solvation shell despite its comparatively low content in the electrolyte (PF_6^- : FSI^- = 1 : 40) (Fig. 5h). PF_6^- participating in the formation of the solvation structure can compete for oxidative decomposition on the cathode surface, contributing to the construction of a more robust CEI, as confirmed by the XPS results. This increases the structural stability of the cathode during charge/discharge cycling, avoiding microcrack formation and/or the surface reconstruction of cathode particles, both of which deteriorate performance.

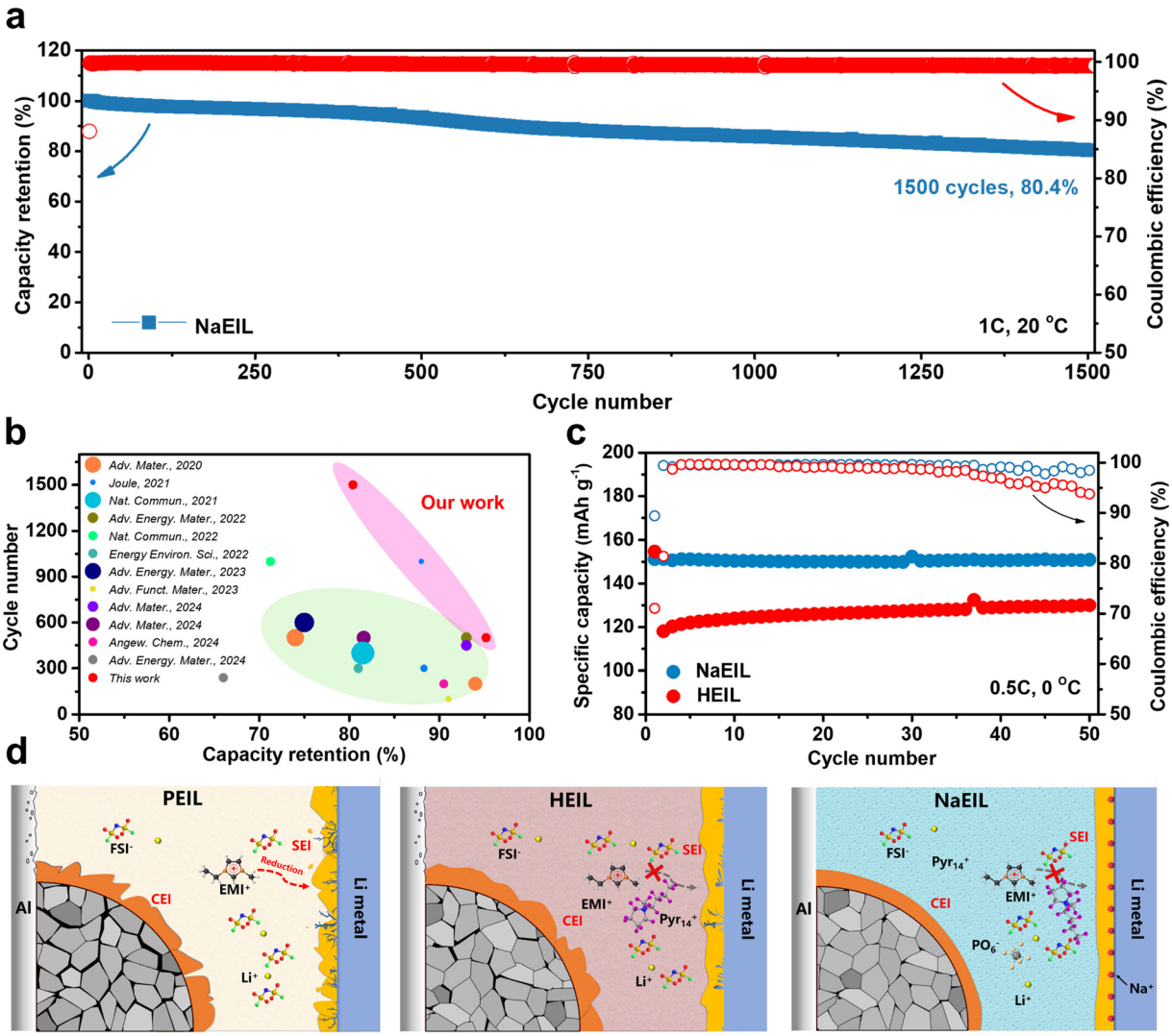

Fig. 6 (a) Long-term cycling behaviour of the Li||NCM83 cell with NaEIL at 20 °C. (b) Comparison with reported state-of-the-art IL-based and additive-assisted electrolytes in nickel-rich cathodes (the size of the circles is proportional to the areal current density). (c) Cycling performance of Li||NCM83 cells with HEIL and NaEIL at 0 °C. (d) Schematic of the effects of PEIL, HEIL and NaEIL electrolytes on the secondary cathode particles in Li||NCM83 cells.

On the anode side, however, the strong adsorption energy of FSI^- on the lithium surface (−2.2 eV) supports its preferential involvement in the SEI formation (Fig. 5i, corresponding adsorption models are displayed in Fig. S20, ESI†). The large steric hindrance of Pyr_{14}^+ and the strong adsorption energy of anions (FSI^- and PF_6^-) restrict the access of EMI^+ cations to the lithium surface, preventing its reduction and thereby leading to the superior cathodic stability of the electrolyte.

To further highlight the outstanding electrochemical stability induced by the $NaPF_6$ electrolyte additive for nickel-rich cathodes in lithium metal cells, the NaEIL cells were subjected to long-term cycling tests. As shown in Fig. 6a, the Li|NaEIL|NCM83 cell maintains high cycling stability after 1500 cycles at a charge/discharge rate of 1C (0.5 mA cm^{-2}), with a capacity retention of >80%. This remarkable performance is superior to most previous reported IL-based cells in terms of the cycle life and rate performance (Fig. 6b; for details, see Table S1, ESI†),[9,25,48–56] and it indicates the great potential of the designed ILE for high-specific-energy lithium metal cells. Finally, to evaluate the performance of the ILEs at lower temperatures, Li||NCM83 cells were tested at 0 °C (Fig. 6c). While the HEIL-based cell delivers a capacity of ~120 mA h g^{-1} at 0.5C (0.25 mA cm^{-2}), its CE declines after 30 cycles. By contrast, the NaEIL cell delivers a capacity of 150 mA h g^{-1}, *i.e.*, slightly more than its 80% discharge capacity delivered at 20 °C, and maintains a stable CE upon cycling. These results demonstrate the remarkable low-temperature performance of the NaEIL, contrasting the typical behaviour of common ionic liquid-based electrolytes at subambient temperatures.

In summary, while the pure EMI-based ILE suffers from poor lithium metal compatibility, which is ascribed to the reduction of EMI cations with lithium metal, the presence of Pyr_{14} cations efficiently suppresses this side reaction and lithium dendrite growth. However, by adding $NaPF_6$, which enables the formation of highly uniform and robust electrode/electrolyte interphases, the structural deterioration of the cathode and the growth of lithium dendrites can be fully avoided (Fig. 6d), guaranteeing the high stability of nickel-rich lithium metal batteries even upon long-term cycling.

3. Conclusions

In this work, a novel dual-cation–based ionic liquid electrolyte is designed. Li||NCM83 cells operating with this electrolyte achieve high cycling stability with a capacity retention of 95.2% after 500 cycles at 1C. The addition of $NaPF_6$ demonstrates great advantages by tuning the electrode/electrolyte interphases. On the one hand, the larger Na^+ is co-deposited, which facilitates uniform lithium deposition. On the other hand, PF_6^- is involved in the solvation structure of lithium ions and contributes to the formation a robust inorganic-rich cathode–electrolyte interphase, which helps prevent microcrack formation and lattice distortion in the secondary and primary cathode particles, respectively. This study reports the $NaPF_6$ additive strategy for developing high-performance ionic liquid-based electrolytes, as well as other electrolyte, for high-voltage nickel-rich cathodes and provides an in-depth understanding of the principles for designing electrolytes for lithium metal batteries.

4. Experimental section

4.1. Material preparation

The $LiNi_{0.83}Co_{0.11}Mn_{0.05}B_{0.01}O_2$ (NCM83) positive electrode was prepared by mixing the active material, conductive carbon Super C65 (IMERYS) and polyvinylidene difluoride binder (PVdF, Solef 6020, Solvay) in a weight ratio of 92 : 4 : 4 into a slurry (solid content ≥ 60%) using *N*-methyl-2-pyrrolidone (NMP; anhydrous, >99.5%; Sigma-Aldrich) as a dispersant and a solvent. Then, the slurry was cast onto an aluminum foil (12 μm) and dried in a dry room (dew point < −60 °C) overnight. The foil was punched into 12-mm-diameter disks, which were vacuum-dried at 120 °C for 12 h and then pressed at 5 ton cm^{-2}. The average areal loading was approximately 2.5 mg cm^{-2}. The ionic liquid electrolytes were prepared by dissolving LiFSI (LiFSI, 99%, PROVISCO, CS) in EMIFSI in a molar ratio of 2 : 8 or by mixing LiFSI with EMIFSI and $Pyr_{14}FSI$ in a molar ratio of 2 : 4 : 4. Both ILs were prepared in-house according to the procedure described in the literature.[57] Next, the electrolytes were pre-dried in a tubular vacuum oven (Büchi) at 70 °C and further purified by pumping down until 10^{-7} mbar using a turbo molecular pump to remove volatile compounds. The water content of the ILs and electrolytes was below 10 ppm, as determined *via* Karl–Fischer titration. The NaEIL electrolyte was prepared by dissolving LiFSI and $NaPF_6$ in EMIFSI and $Pyr_{14}FSI$ in a molar ratio of 0.2 : 1.8 : 4 : 4.

4.2. Electrochemical measurements

Galvanostatic cycling was conducted in pouch cells, which were assembled in a dry room (dew point < −60 °C) using Whatman glass fibre sheets (GF/A) as separators and lithium metal sheets as the counter electrode (500 μm thick, 2 cm × 2 cm size). The cells were cycled between 3.0 V and 4.3 V at 0.1C during the first two (formation) cycles and then at 1C in the Maccor battery tester 4300. The anodic electrochemical stability of all electrolytes was evaluated *via* linear sweep voltammetry (Solartron 1260) using platinum as the working electrode and Li metal as the counter electrode in a Swagelok® type T-cell. The cell voltage was swept at 0.1 mV s^{-1} from the open circuit value (OCV) towards more positive (anodic) voltages. The electrochemical impedance spectroscopy (EIS) of Li-metal cells was performed using a VMP multichannel potentiostat (Bio-Logic). Impedance spectra were collected from cells in a fully discharged state in the frequency range from 1 MHz to 10 mHz by applying a 5-mV voltage amplitude. The (dis)charge rate of 1C corresponds to a specific current of 200 mA g^{-1}. All potential values from three-electrode cells refer to the Li/Li^+ quasi-reference redox couple. Unless otherwise indicated, all electrochemical measurements were performed in climatic chambers set at 20 ± 2 °C.

4.3. Materials characterization

The conductivity of ILEs was measured using a conductometer equipped with a frequency analyser and a thermostatic bath

(MMates Italia). The electrolytes were sealed in glass conductivity cells (assembled in the glove box) equipped with two platinum-platinized electrodes. The cell constant was determined using a 0.01 M KCl standard solution. The corresponding measurements were performed in the temperature range from −30 to 80 °C and recorded every 5 °C. The equilibration time at each temperature was set to 1 h.

The morphologies of electrodes were investigated *via* scanning electron microscopy (SEM; ZEISS Crossbeam XB340 equipped with an energy-dispersive X-ray spectroscopy (EDX) detector). To investigate the internal structure of the electrode and crystal structure of cathode particles, the samples were etched using a Capella focused ion-beam (FIB) source (gallium ion source) using milling and polishing currents of 30 nA and 3 nA, respectively, at an acceleration voltage of 30 kV. Then, the cross-sections of samples were investigated *via* spherical-aberration-corrected scanning transmission electron microscopy (Cs-STEM, Titan Cubed Themis G2300) with EDX (Super X, 300 kV). ToF-SIMS measurements were conducted on positive electrodes after 200 cycles to study their chemical composition as a function of the sample depth. A Cs^+ beam (~70 nA at 2 keV) was employed to sputter a 100 × 100 μm^2 area. X-ray photoelectron spectroscopy (XPS) was performed using a Specs XPS system with a Phoibos 150 energy analyzer using monochromatic Al Kα radiation (1486.6 eV) and pass energies of 30 and 90 eV at the analyzer for detail and survey spectra, respectively. The XPS analysis of samples was performed either directly or after Ar^+ ion sputtering for 30 min (sputtering rate = ~0.1 nm min^{-1}, 0.03 μA, 5 kV). Casa XPS was used for data analysis, applying Shirley-type backgrounds and Gaussian–Lorentzian peak shapes. For the p peaks (P 2p and S 2p), peak doublets with the expected intensity ratio (2 : 1) and spin–orbit splitting(s) were used in the fit. All XPS spectra were calibrated to the C (1s) peak of the adventitious C (C–C/C–H species)/conductive C additive at 284.8 eV. For sample preparation, all cycled electrodes were thoroughly rinsed with DMC, vacuum-dried, and transferred to the characterization equipment under inert gas.

X-ray diffraction (XRD) patterns were recorded using a Bruker D8 diffractometer equipped with a Cu Kα source (λ = 0.15406 nm) in the $10^\circ < 2\theta < 140^\circ$ range with a step size of 0.010° and an acquisition time of 1.4 s per point for powder samples, while the *in situ* datasets were acquired in the $10^\circ < 2\theta < 88.5^\circ$ range with a step size of 0.022° and an acquisition time of 0.5 s per point.

Operando XRD experiments were performed using the same Bruker D8 diffractometer to measure the unit cell evolution and phase transition during (dis)charge. The patterns were collected in the 2θ range from 16° to 73° with a step size of 0.0164°. The operando tests were conducted in the voltage range from 4.3 V to 3.0 V at a charge rate of 0.04C and a discharge rate of 0.06C with a sampling interval time of 30 minutes. The collected XRD patterns were refined in the $R\bar{3}m$ space group[58] using the Le Bail method and the JANA 2020 software.[59] The refinement settings include a manually defined background in combination with the Chebyshev polynomial with five variables. Subsequently, the vertical shift was considered using Sycos, while the unit cell parameters (a and c) were refined. The peak profile was refined using the pseudo-Voigt peak-shape function with GW, LY, and LX.

Molecular dynamics (MD) simulations were used to investigate the solvation structures of electrolytes (representative solvent structure snapshots are shown in Fig. S19, ESI†). For the HEIL system, the simulation comprised 100 LiFSI, [Pyr_{14}][FSI] and [EMI][FSI] in a ratio 2 : 4 : 4. For the NaEIL system, the simulation comprised 100 LiFSI, [Pyr_{14}][FSI], [EMI][FSI] and $NaPF_6$ in a ratio 1.8 : 4 : 4 : 0.2. The solution components were randomly packed into cubic simulation boxes. All MD simulations were performed using the Forcite module with the COMPASS III force field[60] in Materials Studio (MS) 2020. van der Waals and Coulombic interactions were respectively considered by atom-based and Ewald methods with a cut-off value of 12.5 Å. Equations of motion were integrated with a time step of 1 fs. After energy minimization, the electrolyte system was fully relaxed under periodic boundary conditions for 400 ps in the NPT (P = 1 atmosphere, T = 293.0 K) ensemble using the Nose thermostat and Berendsen barostat, which was sufficient time for the system temperature, potential and total energy to stabilize. After reaching the equilibrium state, another 400-ps simulation under the NVT ensemble was performed to extract trajectory and data for calculating the radial distribution function (RDF) and coordination number (CN). The dynamic trajectory for each system was outputted at an interval of 4 ps. The coordination number N_i of atom i in the first solvation shell surrounding Li^+ was calculated as follows:

$$N_i = 4\pi\rho\int_0^{R_M} g(r)r^2 dr$$

where R_M is the distance of the first minimum following the first peak in the RDF curve, $g(r)$ represent the RDF curve, ρ is the number density of atom i. The binding energies between Li^+ and FSI^- or PF_6^- as well as the HOMOs and LUMOs of LiFSI, [Pyr_{14}][FSI], [EMI][FSI] and $NaPF_6$ were calculated using the DMOL3 module in MS 2020 in MS. Firstly, the generalized gradient approximation (GGA) with the Perdew–Burke–Ernzerhof (PBE) exchange–correlation functional was employed to fully relax FSI^-, PF_6^-, LiFSI, [Pyr_{14}][FSI], [EMI][FSI] and $NaPF_6$. The double-numeric quality basis sets with polarization functions were used. The iterative tolerances for energy change, force and displacements were 1 × 10^{-5} Ha, 0.002 Ha $Å^{-1}$ and 0.005 Å, respectively. In the self-consistent field (SCF) procedure, 10^{-6} a.u. was used for the convergence standard electron density. After structural optimization, the Adsorption Locator Tools[61] in MS were used to locate Li^+ at the energy favourable site of FSI^- and PF_6^-. Then, each interaction pair was freely optimized using the DMol3 module. Finally, single-point energy calculations were executed. The binding energies E_b were calculated using the following equation:

$$E_b = E_{total} - E_{anion} - E_{Li^+}$$

where E_{total} is the total energy of the optimized adsorption structure, E_{anion} is the energy of FSI^- or PF_6^-, and E_{Li^+} is the energy of one Li^+.

The calculations for EMI^+, Pyr_{14}^+, FSI^- and PF_6^- adsorption on the Li (100) surface were respectively performed within the framework of the density functional theory (DFT) as implemented in the Vienna *Ab-initio* Simulation Package (VASP) code using the projector-augmented wave method with the Perdew–Burke–Ernzerhof (PBE) exchange–correlation functional.[62] The influence of vdW interactions was considered using a modified version of vdW-DF, referred to as "optB86b-vdW".[63] The projector-augmented wave potentials were used with an energy cut-off of 500 eV. The lattice constraints for the Li (100) slab, which is composed of four layers Li, are 13.775 Å × 13.775 Å. There exists a vacuum layer larger than 20 Å perpendicular to the surface plane. A 3 × 3 × 1 Monkhorst *k*-mesh was used for geometry optimization, during which the bottom layer of the Li substrate was fixed. An energy convergence of 1.0×10^{-4} meV per atom was ensured during self-consistent field calculations. The convergence criterion for the atomic forces was 0.01 eV $Å^{-1}$. After structural optimization, EMI^+, Pyr_{14}^+, FSI^- and PF_6^- were respectively adsorbed on the Li (100) surface. Then, geometrical optimization was performed for each adsorption system, followed by static calculations. The *k*-meshes were doubled for single-point calculations. The adsorption energies E_{ad} were calculated using the following equation:

$$E_{ad} = E_{total} - E_{adsorbate} - E_{slab}$$

where E_{total}, $E_{adsorbate}$ and E_{slab} are the energies of the adsorption system, adsorbate, (*i.e.* EMI^+, Pyr_{14}^+, FSI^- or PF_6^-) and Li (100) slab, respectively.

Author contributions

F. W.: conceptualization, investigation, data curation, writing – original draft, funding acquisition. H. T.: supervision, funding acquisition, writing – review & editing. J. W. & H. L.: ToF-SIMS measurements, writing – review & editing. X. X.: *in situ* XRD refinements, writing – review & editing. T. D.: XPS measurements, writing – review & editing. S. F. & H. L. & J. K. K.: writing – review & editing. Z. L. & H. L. & E. X.: data curation. G. T. K.: conceptualization, writing – review & editing. H. T. & S. P.: supervision, funding acquisition, writing – review & editing.

Data availability

The data supporting the findings of this study are available within the article and its ESI.† Additional datasets generated and analyzed for this work are available from the corresponding author upon reasonable request.

Conflicts of interest

The authors declare no competing interest.

Acknowledgements

The authors would like to acknowledge the financial support from the Hubei Provincial Natural Science Foundation of China (2024AFB084), the China Postdoctoral Science Foundation (2024M752502), the National Research Foundation of Korea (NRF) grant funded by the Korea government (MSIT) (No. RS-2023-00217581 and RS-2023-00248824), and the Helmholtz Association.

References

1 W. Li, E. M. Erickson and A. Manthiram, *Nat. Energy*, 2020, **5**, 26–34.
2 A. Manthiram, *Nat. Commun.*, 2020, **11**, 1550.
3 S. Tan, Z. Shadike, J. Li, X. Wang, Y. Yang, R. Lin, A. Cresce, J. Hu, A. Hunt, I. Waluyo, L. Ma, F. Monaco, P. Cloetens, J. Xiao, Y. Liu, X.-Q. Yang, K. Xu and E. Hu, *Nat. Energy*, 2022, **7**, 484–494.
4 C. Zhao, C. Wang, X. Liu, I. Hwang, T. Li, X. Zhou, J. Diao, J. Deng, Y. Qin, Z. Yang, G. Wang, W. Xu, C. Sun, L. Wu, W. Cha, I. Robinson, R. Harder, Y. Jiang, T. Bicer, J.-T. Li, W. Lu, L. Li, Y. Liu, S.-G. Sun, G.-L. Xu and K. Amine, *Nat. Energy*, 2024, **9**, 345–356.
5 F. Wu, A. Mullaliu, T. Diemant, D. Stepien, T. N. Parac-Vogt, J. K. Kim, D. Bresser, G. T. Kim and S. Passerini, *InfoMat*, 2023, **5**, e12462.
6 N. T. T. Tran, C.-a Lin and S.-k Lin, *ACS Sustainable Chem. Eng.*, 2023, **11**, 6978–6987.
7 A. Heist, S. Hafner and S.-H. Lee, *J. Electrochem. Soc.*, 2019, **166**, A873–A879.
8 Y.-K. Sun, *ACS Energy Lett.*, 2019, **4**, 1042–1044.
9 F. Wu, S. Fang, M. Kuenzel, A. Mullaliu, J.-K. Kim, X. Gao, T. Diemant, G.-T. Kim and S. Passerini, *Joule*, 2021, **5**, 2177–2194.
10 T. Weigel, F. Schipper, E. M. Erickson, F. A. Susai, B. Markovsky and D. Aurbach, *ACS Energy Lett.*, 2019, **4**, 508–516.
11 T. Deng, X. Fan, L. Cao, J. Chen, S. Hou, X. Ji, L. Chen, S. Li, X. Zhou, E. Hu, D. Su, X.-Q. Yang and C. Wang, *Joule*, 2019, **3**, 2550–2564.
12 M. Mao, B. Huang, Q. Li, C. Wang, Y.-B. He and F. Kang, *Nano Energy*, 2020, **78**, 105282.
13 W. Li, Z. He, Y. Jie, F. Huang, Y. Chen, Y. Wang, W. Zhang, X. Zhu, R. Cao and S. Jiao, *Adv. Funct. Mater.*, 2024, **34**, 2406770.
14 J. Xu, *Nano-Micro Lett.*, 2022, **14**, 166.
15 X. Zheng, L. Huang, W. Luo, H. Wang, Y. Dai, X. Liu, Z. Wang, H. Zheng and Y. Huang, *ACS Energy Lett.*, 2021, **6**, 2054–2063.
16 S. Liu, X. Ji, N. Piao, J. Chen, N. Eidson, J. Xu, P. Wang, L. Chen, J. Zhang, T. Deng, S. Hou, T. Jin, H. Wan, J. Li, J. Tu and C. Wang, *Angew. Chem.*, 2021, **60**, 3661–3671.
17 E. P. Kamphaus, S. Angarita-Gomez, X. Qin, M. Shao, M. Engelhard, K. T. Mueller, V. Murugesan and P. B. Balbuena, *ACS Appl. Mater. Interfaces*, 2019, **11**, 31467–31476.
18 K. Xu, *Chem. Rev.*, 2014, **114**, 11503–11618.

19 Y. S. Meng, V. Srinivasan and K. Xu, *Science*, 2022, **378**, eabq3750.
20 F. Wu, G. T. Kim, T. Diemant, M. Kuenzel, A. R. Schür, X. Gao, B. Qin, D. Alwast, Z. Jusys, R. J. Behm, D. Geiger, U. Kaiser and S. Passerini, *Adv. Energy Mater.*, 2020, **10**, 2001830.
21 J. Li, W. Li, Y. You and A. Manthiram, *Adv. Energy Mater.*, 2018, **8**, 1801957.
22 F. Wu, Z. Chen, S. Fang, W. Zuo, G.-T. Kim and S. Passerini, *Energy Storage Mater.*, 2023, **63**, 103062.
23 X. Wang, M. Salari, D.-E. Jiang, J. Chapman Varela, B. Anasori, D. J. Wesolowski, S. Dai, M. W. Grinstaff and Y. Gogotsi, *Nat. Rev. Mater.*, 2020, **5**, 787–808.
24 S. Brutti, E. Simonetti, M. De Francesco, A. Sarra, A. Paolone, O. Palumbo, S. Fantini, R. Lin, A. Falgayrat, H. Choi, M. Kuenzel, S. Passerini and G. B. Appetecchi, *J. Power Sources*, 2020, **479**, 228791.
25 H. Sun, G. Zhu, Y. Zhu, M. C. Lin, H. Chen, Y. Y. Li, W. H. Hung, B. Zhou, X. Wang, Y. Bai, M. Gu, C. L. Huang, H. C. Tai, X. Xu, M. Angell, J. J. Shyue and H. Dai, *Adv. Mater.*, 2020, **32**, e2001741.
26 P. Schmitz, R. Jakelski, M. Pyschik, K. Jalkanen, S. Nowak, M. Winter and P. Bieker, *ChemSusChem*, 2017, **10**, 876–883.
27 T. Hosokawa, K. Matsumoto, T. Nohira, R. Hagiwara, A. Fukunaga, S. Sakai and K. Nitta, *J. Phys. Chem. C*, 2016, **120**, 9628–9636.
28 M. Egashira, H. Todo, N. Yoshimoto, M. Morita and J.-I. Yamaki, *J. Power Sources*, 2007, **174**, 560–564.
29 J. M. Klein, E. Panichi and B. Gurkan, *Phys. Chem. Chem. Phys.*, 2019, **21**, 3712–3720.
30 M. Lazzari, M. Mastragostino and F. Soavi, *Electrochem. Commun.*, 2007, **9**, 1567–1572.
31 J. Chen, Y. Zhang, H. Lu, J. Ding, X. Wang, Y. Huang, H. Ma and J. Wang, *eScience*, 2023, **3**, 100135.
32 C. Fang, J. Li, M. Zhang, Y. Zhang, F. Yang, J. Z. Lee, M.-H. Lee, J. Alvarado, M. A. Schroeder, Y. Yang, B. Lu, N. Williams, M. Ceja, L. Yang, M. Cai, J. Gu, K. Xu, X. Wang and Y. S. Meng, *Nature*, 2019, **572**, 511–515.
33 L. de Biasi, A. Schiele, M. Roca-Ayats, G. Garcia, T. Brezesinski, P. Hartmann and J. Janek, *ChemSusChem*, 2019, **12**, 2240–2250.
34 R.-S. Kühnel and A. Balducci, *J. Power Sources*, 2014, **249**, 163–171.
35 X. Zhang, B. Winget, M. Doeff, J. W. Evans and T. M. Devine, *J. Electrochem. Soc.*, 2005, **152**, B448.
36 S. Qi, X. Tang, J. He, J. Liu and J. Ma, *Small Methods*, 2023, **7**, 2201693.
37 F. Cheng, M. Cao, Q. Li, C. Fang, J. Han and Y. Huang, *ACS Nano*, 2023, **17**, 18608–18615.
38 J. K. Stark, Y. Ding and P. A. Kohl, *J. Electrochem. Soc.*, 2013, **160**, D337.
39 Q. Xu, Y. Yang and H. Shao, *Electrochim. Acta*, 2018, **271**, 617–623.
40 D. Monti, E. Jónsson, M. R. Palacín and P. Johansson, *J. Power Sources*, 2014, **245**, 630–636.
41 J. K. S. Goodman and P. A. Kohl, *J. Electrochem. Soc.*, 2014, **161**, D418.
42 Y. You, H. Celio, J. Li, A. Dolocan and A. Manthiram, *Angew. Chem.*, 2018, **57**, 6480–6485.
43 Z. Wang, Z. Wang, D. Xue, J. Zhao, X. Zhang, L. Geng, Y. Li, C. Du, J. Yao, X. Liu, Z. Rong, B. Guo, R. Fang, Y. Su, C. Delmas, S. J. Harris, M. Wagemaker, L. Zhang, Y. Tang, S. Zhang, L. Zhu and J. Huang, *Nano Energy*, 2023, **105**, 108016.
44 X. Pu, S. Zhang, D. Zhao, Z.-L. Xu, Z. Chen and Y. Cao, *Electrochem. Energy Rev.*, 2024, **7**, 21.
45 J. Wang, L. Li, H. Hu, H. Hu, Q. Guan, M. Huang, L. Jia, H. Adenusi, K. V. Tian, J. Zhang, S. Passerini and H. Lin, *ACS Nano*, 2022, **16**, 17729–17760.
46 C. Yang, X. Liao, X. Zhou, C. Sun, R. Qu, J. Han, Y. Zhao, L. Wang, Y. You and J. Lu, *Adv. Mater.*, 2023, **35**, 2210966.
47 B.-H. Zhang, P.-P. Chen, Y.-L. Hou, J.-Z. Chen, H.-Y. Wang, W.-X. Wen, Z.-A. Li, J.-T. Lei and D.-L. Zhao, *Small*, 2024, **20**, 2402123.
48 W. Zou, J. Zhang, M. Liu, J. Li, Z. Ren, W. Zhao, Y. Zhang, Y. Shen and Y. Tang, *Adv. Mater.*, 2024, **36**, 2400537.
49 Y. Li, F. Ding, Y. Shao, H. Wang, X. Guo, C. Liu, X. Sui, G. Sun, J. Zhou and Z. Wang, *Angew. Chem., Int. Ed.*, 2024, **63**, e202405648.
50 K. Ding, E. J. Begin, S. Yuan, M. Zhong, Y. Wang, Y. Zhang, X. Zeng, J. L. Bao and Y. Wang, *Adv. Energy Mater.*, 2023, **13**, 2302443.
51 X. Liu, A. Mariani, T. Diemant, M. E. Di Pietro, X. Dong, A. Mele and S. Passerini, *Adv. Mater.*, 2023, **36**, 2309062.
52 X. Liu, A. Mariani, T. Diemant, M. E. D. Pietro, X. Dong, M. Kuenzel, A. Mele and S. Passerini, *Adv. Energy Mater.*, 2022, **12**, 2200862.
53 D. Zhang, M. Liu, J. Ma, K. Yang, Z. Chen, K. Li, C. Zhang, Y. Wei, M. Zhou, P. Wang, Y. He, W. Lv, Q. H. Yang, F. Kang and Y. B. He, *Nat. Commun.*, 2022, **13**, 6966.
54 Z. Wang, R. Han, H. Zhang, D. Huang, F. Zhang, D. Fu, Y. Liu, Y. Wei, H. Song, Y. Shen, J. Xu, J. Zheng, X. Wu and H. Li, *Adv. Funct. Mater.*, 2023, **33**, 2215065.
55 J. Forero-Saboya, I. A. Moiseev, M. L. Vlara, D. Foix, M. Deschamps, A. M. Abakumov, J. M. Tarascon and S. Mariyappan, *Adv. Energy Mater.*, 2024, **14**, 2402051.
56 S. Park, S. Y. Jeong, T. K. Lee, M. W. Park, H. Y. Lim, J. Sung, J. Cho, S. K. Kwak, S. Y. Hong and N.-S. Choi, *Nat. Commun.*, 2021, **12**, 838.
57 M. Montanino, F. Alessandrini, S. Passerini and G. B. Appetecchi, *Electrochim. Acta*, 2013, **96**, 124–133.
58 X. Zheng, X. Li, B. Zhang, Z. Wang, H. Guo, Z. Huang, G. Yan, D. Wang and Y. Xu, *Ceram. Int.*, 2016, **42**, 644–649.
59 V. Petříček, L. Palatinus, J. Plášil and M. Dušek, *Z. Kristallogr. - Cryst. Mater.*, 2023, **238**, 271–282.
60 H. Sun, P. Ren and J. Fried, *Comput. Theor. Polym. Sci.*, 1998, **8**, 229–246.
61 Z. Qu, Y. Muhammad, W. He, J. Li, Z. Gao, J. Fu, S. J. Shah, H. Sun, J. Wang and Z. Huang, *Chem. Eng. J.*, 2021, **404**, 126570.
62 G. Kresse and J. Furthmüller, *Phys. Rev. B:Condens. Matter Mater. Phys.*, 1996, **54**, 11169.
63 J. Klimeš, D. R. Bowler and A. Michaelides, *J. Phys.: Condens. Matter*, 2009, **22**, 022201.

